Mechatronics 23 (2013) 397–408

Contents lists available at SciVerse ScienceDirect

Mechatronics

journal homepage: www.elsevier.com/locate/mechatronics

# Design and FE analysis of integrated sensing using gas compressibility for microdroplet generation

William Rone, Pinhas Ben-Tzvi *

*Robotics and Mechatronics Laboratory, Department of Mechanical and Aerospace Engineering, The George Washington University, Washington, DC, USA*

ARTICLE INFO

*Article history:*
Received 17 May 2011
Accepted 3 March 2013
Available online 30 March 2013

*Keywords:*
MEMS
Microfluidics
Droplet generation
Compressible flow
Finite element analysis
COMSOL Multiphysics

ABSTRACT

As trends in biology, chemistry, medicine and manufacturing have pushed macroscopic processes onto the microscale, robust technologies have become necessary to encapsulate liquids into microdroplets for further manipulation and use. In order to most effectively utilize these microdroplets, real-time sensing is needed during the generation process to monitor the size of the droplet generated, or if generation failed to occur. Current droplet generating technologies operate either in open-loop, with no direct feedback available to the control system to monitor the process, or in closed loop with external sensing, using photography or droplet weight measurement to measure droplet size. By utilizing internal system-based sensing to close the loop, corrections in the dispensing process could be made in real-time in response to malfunctions as they occur. Furthermore, the generator's operator could be more quickly alerted when a systemic error, such as a clog, continues to occur. One candidate solution to provide system-based sensing is to monitor the pressure of a reservoir of compressible gas kept adjacent to the reservoir of droplet liquid, both within a constant volume fluid chamber. The gas reservoir pressure during the actuation sequence can be related both analytically and empirically to the volume of the droplet ejected from the device, including instances where generation fails and a droplet is not ejected. This paper describes the designs of potential systems to realize this design concept, and the development of a finite element simulation for one of the concepts capable of generating droplets while simultaneously monitoring the pressure of the gas reservoir. A linear relationship between this calculated pressure and the volume of the dispensed droplet is found, validating the sensible property as workable for implementation in a physical system.



## 1. Introduction

As microdroplet generators have developed from novel concepts to critical laboratory instruments, two considerations have dominated the academic research and commercial development in the field. The first consideration has been reducing droplet size in order to allow further miniaturization and more efficient use of the dispensing liquid. The second consideration has been the development of novel actuation mechanisms to more efficiently and/or quickly generate droplets. However, device-based real-time monitoring and measurement of droplet generation has seen minimal study and less implementation.

As researchers have pushed droplet diameters below the micrometer range and developed innovative actuation mechanisms for producing droplets, a new focus on designing integrated systems capable of robust feedback control is the next frontier for developing precision lab automation devices capable of sub-picoliter droplet dispensing. A first step in developing this type of system is to determine a sensible property that will indirectly allow the size of a generated droplet to be measured and monitored by the control system, and to develop system designs capable of simultaneously sensing this property and actuating generation.

This paper is organized as follows: Section 2 provides background on the field of microdroplet generation and a proposed system design concept to address current shortcomings. Section 3 describes the finite element model used for the multi-phase compressible air gap simulations performed. Section 4 presents the results from the simulations and related analysis. Section 5 outlines the conclusions and highlights potential areas for future development.

## 2. Background and design concept

Lord Rayleigh pioneered the field of droplet generation in 1878, where he modeled the breakup of a liquid jet into a continuous stream of droplets [1]. A century later, companies including Clevite [2], Silonics [3], Canon [4] and Hewlett–Packard [5] developed

* Corresponding author. Tel.: +1 202 994 6149; fax: +1 202 994 0238.
*E-mail address:* bentzvi@gwu.edu (P. Ben-Tzvi).

0957-4158/$ - see front matter © 2013 Elsevier Ltd. All rights reserved.
http://dx.doi.org/10.1016/j.mechatronics.2013.03.001

**Nomenclature**

| | | | |
|---|---|---|---|
| $\boldsymbol{F}$ | external force vector (N) | $\gamma$ | reinitialization parameters (unitless) |
| $\boldsymbol{F}_{fr}$ | frictional force vector (N) | $\varepsilon_{ls}$ | interface thickness parameter (m) |
| $\boldsymbol{g}$ | gravity vector (m/s$^2$) | $\theta_w$ | contact angle (rad) |
| $\boldsymbol{n}$ | normal vector (unitless) | $\mu$ | absolute viscosity (Pa·s) |
| $\boldsymbol{u}/\boldsymbol{u}_f$ | fluid velocity vector (m/s) | $\rho$ | density (kg/m$^3$) |
| $\boldsymbol{u}_s$ | solid displacement vector | $\varphi$ | level set variable (unitless) |
| $p$ | pressure (Pa) | | |
| $\beta$ | slip length (m) | | |

drop-on-demand generator using piezoceramic [2,3] and thermal [4,5] actuation. These two actuation mechanisms dominate generators currently used in industry, though other novel actuation concepts have also been developed.

In order to understand the needed improvements to current technologies within the field of microdroplet generation, an understanding of the current actuation mechanisms, sensing techniques and real-world applications is necessary. From this background, the shortcomings of the field are identified and a novel system design is presented to address these shortcomings. For a more extensive assessment of the field, see [6].

### 2.1. Methods and applications of droplet generation

#### 2.1.1. Current actuation mechanisms

Piezoelectric actuators are the most common actuator studied in the literature. They generate a mechanical force in response to a potential difference. They may operate in four modes: (i) push-mode, where the piezo imparts a linear motion to generate a droplet [7,8]; (ii) squeeze-mode, where the piezo expands and contracts to generate a droplet [9]; (iii) bend-mode, where the piezo bends due to constraints at its boundaries to generate droplets [10]; and (iv) shear-mode, where the piezo deflects in shear to generate droplets [11].

Second in prevalence to piezo-actuators, thermal actuators utilize thermal energy to create droplets. Three types of thermal actuators have been studied: (i) thermal bubble, where a heater locally forms a gas bubble to force a droplet out of the nozzle [12]; (ii) thermal spark, where a spark between two wires or lasers rapidly creates a bubble to actuate generation [13]; and (iii) thermal bulking, where thermal expansion of the generator assembly actuates generation [14].

Beyond these two dominant classes, several other strategies have been studied, but the technologies have not made the jump from academic consideration to commercial application. Among these are acoustic actuation [15], pneumatic actuation [16,17], electrostatic actuation [18,19] and electrohydrodynamic actuation [20,21].

#### 2.1.2. Current sensing tools

External instrumentation is the most common method for monitoring the state of droplet generation, including the occurrence of generation and the volumes of droplets dispensed. The most common is photography, where a droplet's volume is extrapolated from 2D images [10,13,15,16,21]. Dispensed volume weight measurement utilizes a microbalance to weigh droplets as they are produced, accounting for evaporation that may occur, and correlating that weight to the droplets' volumes [22]. Fluorescence spectroscopy measures the fluorescence of deposited droplets and utilizes a calibration curve to determine the volume of fluid dispensed from this signal [23]. Laser Doppler anemometry utilizes the frequency shift observed when a droplet passes two laser beams crossed at a sharp angle to calculate the volume of the droplet [24]. Capacitance sensing detects droplet ejection by measuring the change in the capacitance between a pair of plates as droplet(s) pass through [25].

Integrated sensing is less common in generator system design, where sensing is intrinsically coupled to the generator's design. Optical sensing has been utilized with contact droplet generators, to measure the light passing through the droplet as it is dispensed. Those changes can then be correlated to either a successful or failed attempt at generation [26]. Capacitive sensors have been utilized to measure pressure in the liquid reservoir, to measure displacement of the intermediate membrane in a piezo-actuated generator, and to measure the liquid level in the fluid chamber. These sensors provide closed-loop monitoring of clogging, reduce hysteresis/drift in the piezo and monitor the liquid in the fluid chamber [27,28]. Furthermore, the sensing properties of piezo actuators have also been studied to monitor deposition [29].

#### 2.1.3. Current and future applications

In biological/chemical synthesis/analysis, a promising application of microdroplet generation is DNA and protein microarray generation, where generators either deposit previously synthesized DNA/proteins on a substrate or synthesize DNA *in situ* on the substrate itself [26,30–33]. A second application pertains to preparing samples for mass spectrometry, particularly for protein identification, where the generator discretizes the liquid into sizes suitable for analysis [22,34,35]. A third application is solid support creation and modification, where materials are printed to create/modify support structures to facilitate bioactive molecule attachment or to create transient-release flow obstructions [33].

In medicine, therapeutic and regenerative fields utilize droplet generation. In therapeutics, drug delivery/therapy both orally [24,33,36] and transdermally [37] rely on droplet generation to reliably discretize samples. In regenerative medicine, tissue engineering utilizes generators to dispense biopolymers and cells to form three-dimensional structures and to use growth factors to engineer a more vascular form.

In manufacturing, one application of droplet generation relates to surface coating with materials such as photoresist or electroluminescent polymer [38–40]. A second application relates to creating electrical components, such as transistors and capacitors, from materials including polymers and metallic particles [39,41]. Additionally, net-form manufacturing is driven by droplet generation, where materials such as molten metal [42] and ice [43] are built into desired products.

### 2.2. Shortcomings in current droplet generation technology

Based on the state-of-the-art, there is a shortcoming in device-based integrated sensing. This leads to an over-emphasis on open-loop and vision-based closed-loop control systems. However, each of these control approaches exhibits major flaws.

In open-loop controlled systems, there is no mechanism to correlate the generator's actuation and response. Ideally, a droplet of desired size will eject each time; however, external disturbances (e.g., a change in temperature) or internal faults (e.g., a clog) may cause droplet size irregularities or deposition failures. While one or two of these errors may not have a significant effect, their unchecked accumulation will.

In vision-based closed-loop controlled systems, the size of cameras required to capture droplet images drastically limits the number of dispensers that can be arranged in parallel. Furthermore, most vision systems are based on the stroboscopic effect, where numerous images are overlain to create a composite image. This composite prevents isolation of a disturbance/fault within a single generation cycle, lengthening the time required to correct this error and increasing the error's effects.

These shortcomings are seen in several commercial droplet generators currently on the market. One such generator is the GeSiM [44] SPIP generator, shown in Fig. 1a. Actuation is generated by a bend-mode piezo placed adjacent to the liquid reservoir, with no integrated sensing. A camera may be integrated with the device's control system. However, as seen in Fig. 1b, the scale of the camera is larger than the generator itself and much larger than the nozzle, limiting its potential integration with a parallel array of generators.

Furthermore, as previously discussed, the camera's stroboscopic operation hampers its use. Typical composite stroboscopic images are shown in Fig. 2. The overlay of multiple droplet images creates a "haze" around the droplet. This haze is analogous to a probability distribution of the droplet shape, with darker areas more likely part of the shape and lighter areas less likely. While image processing techniques can determine a best estimate of droplet size, it prevents real-time correction of the droplet size at each cycle.

Challenges associated with open-loop and vision-based control can be improved by utilizing closed-loop control with integrated sensing. Compared to open-loop shortcomings, the use of sensing allows for correlation between actuation and response. However, unlike vision-based sensing, integrated sensing would allow for corrections in response to single actuation cycles. In terms of the vision-based shortcomings, integrated sensing allows a more efficient device form factor to be realized.

Beyond the abstract benefits of this new approach, the expanded use of integrated sensing would improve droplet generator performance in a wide variety of applications. Among those discussed in Section 2.1.3, one of the most critically affected would be DNA microarray printing and utilization. When performing complimentary DNA analysis, the amount of liquid deposited on the microarray directly affects the number of potential binding sites for the test molecules during analysis. The test molecules are marked with fluorescent tags, and the relative strength of the fluorescence at each site determines if the test molecules bind to the site, implying a genetic link. Any unknown variability in droplet size would introduce variability in the number of binding sites, potentially masking the connection if a sufficient number of binding sites are not available to provide the minimum required fluorescence. Furthermore, if the deposited volume were known for each site, the relative signal strength of any detected fluorescence could be compared to the deposited volume at the site, creating a relative fluorescence metric that better measures the complementary binding.

### 2.3. Proposed system design capable of closed-loop control

Based on these shortcomings in the state-of-the-art, a novel design concept for enabling integrated sensing in a droplet generator has been developed. This concept is adapted from our previous work in the field [45] to address several of the previous design's feasibility issues.

Fundamentally, the sensing concept requires that two fluids – an incompressible liquid and a compressible gas – be stored in a

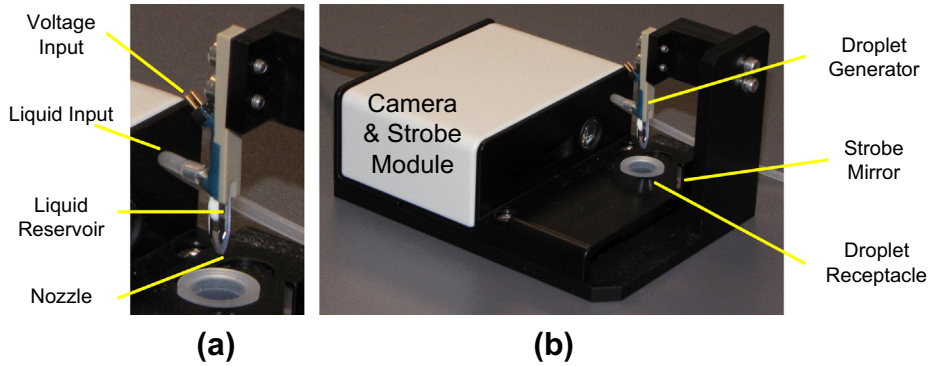


**Fig. 1.** GeSiM SPiP (a) droplet generator, (b) set-up with stroboscope.

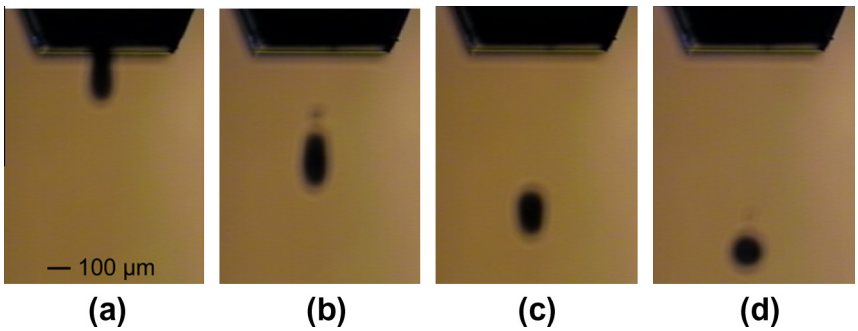


**Fig. 2.** Typical stroboscopic image progression at varying delays from actuation: (a) 100 μs, (b) 200 μs, (c) 300 μs, (d) 400 μs.

single chamber. When an actuator ejects a droplet from the liquid reservoir, the gas reservoir's volume/pressure will change. This pressure change can be related analytically to the dispensed droplet volume, and the analytical calculation can be verified computationally through simulations and empirically by external instrumentation. With this coupling quantified, the integrated sensing closes the loop between the system's actuation and response.

*2.3.1. Mechanical system layout*

Fig. 3 illustrates a potential implementation of the design concept. A capillary is used as the fluid chamber, and a squeeze-mode piezo actuates generation. One end of the capillary incorporates a flow focusing region and nozzle where the droplet ejects, while the opposite end incorporates a flexible cap that seals the gas reservoir. During actuation, the piezo contracts/expands, which deforms the capillary and creates/ejects a droplet at the nozzle. During ejection, the volume of the liquid in the reservoir changes, causing a pressure change in the compressible gas reservoir. This gas pressure change will deform the flexible cap, the deformation of which will measured by a sensor integrated into that cap, such as a piezoceramic or capacitive sensor. A single inlet/outlet is incorporated into the gas reservoir to accommodate aspiration and repressurization (discussed in Section 2.3.2). An inlet/outlet is not possible for the liquid because of its interference with the actuator; the deformation of the fluid chamber would affect the use and/or damage the inlet/outlet.

Fig. 4 illustrates a second implementation. A cylinder is used as the fluid chamber, and an annular squeeze-mode piezo actuates generation. The ends of the fluid chamber consist of a base plate and a flexible cap. The generator's nozzle is aligned with cylinder's axis of symmetry. An annular piezo is attached around the nozzle to deflect the base plate and open the nozzle during actuation, forcing out a droplet of the desired size. As before, a flexible cap with an integrated pressure sensor monitors the gas reservoir pressure changes before, during and after actuation. A pair of inlet/outlet ports is incorporated adjacent to the gas/liquid reservoirs because actuation does not require deformation of the outer shell.

In each design manifestation, the axisymmetricity of the fluid chamber is ruined by the inlet/outlet port(s). However, during development, for many considerations related to modeling and analysis, these ports can be ignored and the device modeled in two dimensions, axisymmetrically.

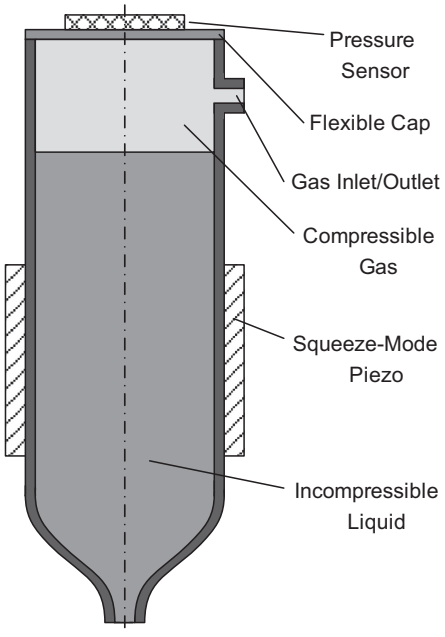


**Fig. 3.** Capillary design manifestation.

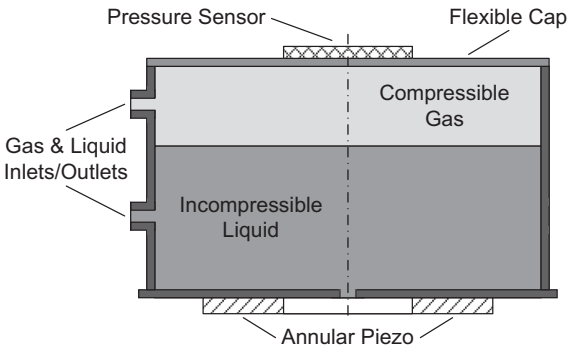


**Fig. 4.** Cylinder design manifestation.

Furthermore, compared to conventional droplet generators, droplet generation will require greater actuation energy, due to the acoustic absorption of the gas during actuation. Implementations of this design will need to account for this higher energy requirement when designing actuation to ensure sufficient pressure will be generated to overcome this energy barrier to ensure droplets are generated and sufficient pressure changes may be measured in the gas reservoir.

*2.3.2. System control concepts*

Fig. 5 shows the data flow between the operator, control system and droplet generator. In terms of operator/control-system interaction, a human operator or a higher-abstraction control system operator will pass to the generator controller a desired quantity of droplets and each of those droplets' desired volume as inputs. As outputs, the control system will pass the actual droplet volume(s) to the operator, during and/or after generation. In terms of control-system/plant interaction, for each droplet, the system controller will command a signal generator to create a voltage pulse to actuate the piezo. During actuation, the pressure sensor will continuously measure the gas pressure, and a signal processor will convert/provide that information to the control system. During repressurization (discussed below), the control system will utilize a pump controller to manipulate the pressure within the system.

Fig. 6 shows the control system logic within the "System Controller" block in Fig. 5. When the system is prompted to generate droplets, an internal counter variable 'i' will initialize to 1 and establish the actuation parameters necessary to generate a droplet of the size required for the initial actuation based on empirical relationships between actuation parameters and droplet size. These parameters will be sent to the droplet generator and a droplet will be ejected. As it is ejected, the pressure sensor's nominal value will be converted into the gas reservoir pressure. This new pressure value will be compared to the previous pressure value, and the difference between these two will be related empirically to the ejected droplet volume. Once the volume is calculated, this value should be provided to the operator. Next, the measured pressure is compared to the empirically determined optimal generation pressure. If the gas reservoir pressure differs from the optimal pressure by too large of an established margin, the system will need to be repressurized. Once the pressure falls within the desired range, if the desired number of droplets has been reached, the process is finished; however, if not, 'i' is incremented and the previous actuation parameters are adjusted, based on the difference between the next desired droplet volume and the previously deposited droplet volume, and the current pressure within the gas reservoir. The actuation parameter adjustment will be based on

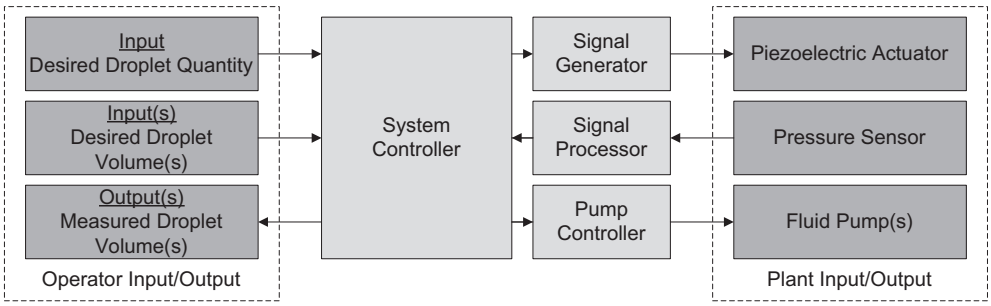


**Fig. 5.** System layout.

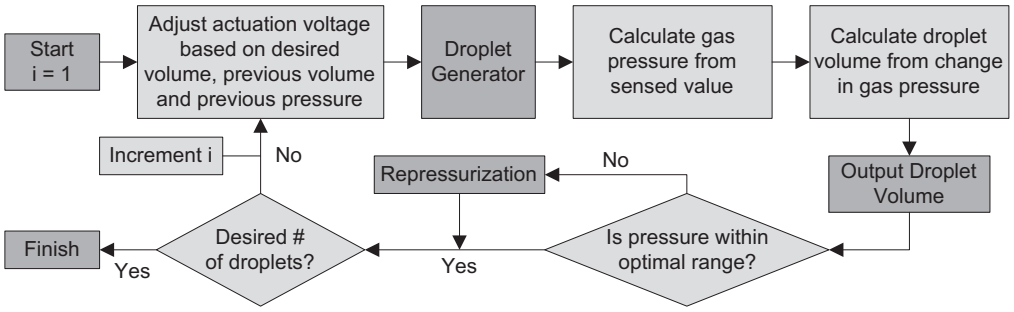


**Fig. 6.** Droplet generator control logic.

empirically determined relationships between the pressure magnitude, volume difference and the actuation parameters.

It should be noted the empirical relationships described will be based on the analytical and numerical relationships found during the design process; however, it is important to verify these empirically to account for unmodeled/unexpected variances from these relations.

Beyond the control system in Fig. 6, there are additional operational modes that must be considered to utilize this device, including repressurization, liquid supplying and misfiring/clogging. To create a droplet, the gas pressure must be within an empirically determined optimal pressure range; if outside this range, repressurization is necessary. Repressurization modifies the gas pressure to within the optimal pressure range to facilitate further generation. It can be achieved by modifying either the liquid or gas. When modifying the gas, liquid volume remains constant and gas is added or vented to modify pressure. When modifying the liquid, liquid is added or removed to adjust the pressure in gas reservoir, keeping the gas reservoir at a constant volume.

The liquid supply mode encompassed how droplet liquid is provided to the system. The capillary design manifestation will use aspiration-mode liquid supply, where liquid is pulled into the generator through the nozzle. The gas inlet/outlet will be used to pull the liquid in. After a fixed reduction of the liquid reservoir volume, the system will return to the liquid source and aspirate. The cylindrical design manifestation will use flow-in-mode liquid supply, where liquid flows directly from the source to the generator. Liquid supplying and repressurization would occur simultaneously; whenever the gas pressure falls out of optimal range, liquid could be added to the system to repressurize, achieving both goals simultaneously.

For robust operation, the generator's liquid reservoir should not have any gas bubbles within it. Preventing this is especially critical during initialization, when the generator initially fills with liquid, and is a common operational issue amongst current droplet generators. The presence of a gas reservoir is not anticipated to introduce bubbles into the liquid reservoir during operation; however, this hypothesis will be verified empirically during development. Furthermore, in future work, selection criteria for the compressible gas will be determined to enable the best gas choice corresponding to a given dispensing liquid.

The third operational mode to be accounted for is misfiring or clogging. Misfiring occurs when a droplet fails to eject in response to a single actuation waveform; clogging occurs when a sequence of misfires occurs, implying a systemic failure.

## 3. Finite element model

COMSOL Multiphysics [46] was used to model the capillary design concept manifestation shown in Fig. 3. COMSOL was chosen because of its utility in modeling multiphase flow and its flexibility for including additional physics in future work, including fluid–structure interaction (FSI) or piezoelectric materials. This design manifestation was chosen to allow for an initial investigation of the sensing capability of the compressible gas gap without having to incorporate FSI, a significant complication to the model. Instead, a pressure boundary condition along a segment of the capillary length that mimics the pressure caused by a moving boundary condition can be used to simplify this preliminary study. While this simplification does not capture the velocity of the moving boundary that would couple with the pressure change to generate the droplet, it does serve as a baseline against which future work can be compared. This assumption was validated in COMSOL using a single-phase flow FSI model.

### 3.1. Geometry

A 2D axisymmetric model was chosen to represent the system. Because the squeeze-mode piezoceramic actuation operates in the radial and longitudinal directions and not in the tangential/azimuthal, the subsequent fluid motion has no impetus to circulate

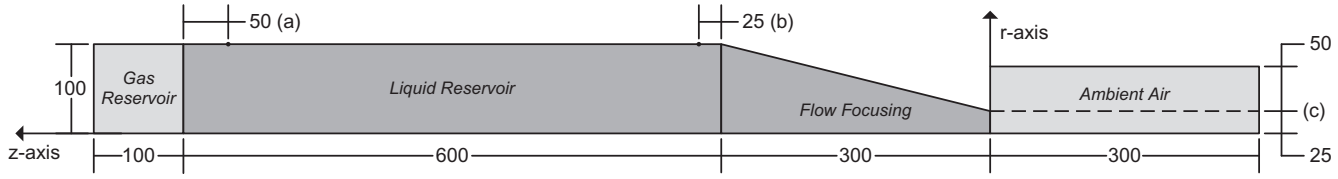


**Fig. 7.** Multi-phase flow model geometry (dimension in micrometers).

around the axis of symmetry. This assumption simplifies the computation without loss of utility. Fig. 7 shows the geometry used to implement the design concept, with the axis of symmetry coinciding with the lower boundary/*z*-axis. An additional simplification was made in defining the flow focusing region with a straight line, as opposed to the curve in Fig. 3. This was to replace the high-density mesh required to define that boundary with a more uniformly transitioning boundary/mesh from the liquid reservoir to nozzle.

The 25 μm dimension for the nozzle radius was the primary constraint on system size. This size was chosen based on the average droplet size of another squeeze-mode piezo-based generator [9]. The region below the nozzle ($z < 0$) was made wide enough to accommodate generation without boundary layer effects. The geometry also defines two points, labeled (a) and (b), for additional boundary condition flexibility, and one segment, labeled (c), control mesh density, as described in Sections 3.3 and 3.4.

### 3.2. Subdomain properties

The COMSOL Material Library was used to model the liquid and gas in the generator. Water was used as the liquid phase because of its common use as a solvent. Air was used in the gas reservoir because of its favorable compressibility properties, and for the region below the nozzle to mimic the ambient environmental conditions. The water–air interface model also defined the interfaces' surface tension. As described in Section 2.3.2, criteria for choosing the proper gas for a given dispending liquid will be developed as part of our future work.

Within these material models, pressure and temperature define the density and viscosity in each fluid. A constant ambient temperature of $T = 25$ °C was used as the temperature input. The pressure input was coupled to the pressure variable $p$. However, because $p$ is a gauge value, 1 atm was added to $p$ to obtain the absolute pressure.

#### 3.2.1. Governing equations

The four dependent variables needed in the fluid model are a velocity vector field $\boldsymbol{u} = [u \quad v \quad w]^T$ and a scalar pressure field $p$.

The Cartesian positions, velocities and accelerations and any subsequent equations or boundary conditions are converted into cylindrical form by COMSOL, with azimuthal terms ignored.

The governing equations for conservation of mass and momentum are used to calculate the pressure and velocity fields. The compressible conservation of mass given by Eq. (1) implies the dilation of any differential volume corresponds to a change in density ($\rho$) in time of that volume. The compressible conservation of momentum given by Eq. (2) equates the sum of the unsteady and convective inertias of the fluid to the sum of the stress divergence ($\nabla \cdot [\ldots]$), the gravitational body force ($\rho \boldsymbol{g}$) and other body forces acting on that differential volume ($\boldsymbol{F}$).

$$\frac{\partial \rho}{\partial t} + \rho \nabla \cdot \boldsymbol{u} = 0 \tag{1}$$

$$\rho \frac{\partial \boldsymbol{u}}{\partial t} + \rho(\boldsymbol{u} \cdot \nabla)\boldsymbol{u} = \nabla \cdot \left[ -p\boldsymbol{I} + \mu(\nabla \boldsymbol{u} + (\nabla \boldsymbol{u})^T) - \frac{2}{3}\mu(\nabla \cdot \boldsymbol{u})\boldsymbol{I} \right] + \rho \boldsymbol{g} + \boldsymbol{F} \tag{2}$$

#### 3.2.2. Interface tracking

The level set method tracks the fluid interfaces by storing the relative composition of each point in a level set variable ($\varphi$) ranging from 0 to 1 ($\varphi = 0 = 100$ gas; $\varphi = 1 = 100$ liquid). Material properties are determined at each node through a weighted combination of the liquid and gas properties.

The level set equation, when coupled to the mass and momentum equations, has the form shown in Eq. (3). The left hand terms conserve the level set variable (note its similarity to Eq. (1)). The right hand terms provide numerical stability, with two parameters controlling numerical stabilization: the reinitialization parameter $\gamma$, and the interface thickness parameter $\varepsilon_{ls}$. $\gamma$ controls the magnitude of the numerical correction, balancing the damping of numerical oscillations (oscillations occur if $\gamma$ is too low) with the need to have the interface accurately tracked (inaccuracies occur if $\gamma$ is too large). $\varepsilon_{ls}$ controls the distance over which the continuous step function that varies from 0 to 1 will occur at the boundaries.

$$\frac{\partial \varphi}{\partial t} + (\boldsymbol{u} \cdot \nabla)\varphi = \gamma \nabla \cdot \left[ \varepsilon_{ls} \nabla \varphi - \varphi(1 - \varphi) \frac{\nabla \varphi}{|\nabla \varphi|} \right] \tag{3}$$

As an initial condition, each subdomain in the model geometry is assigned to have either $\varphi = 0$ (green) or $\varphi = 1$ (red), as shown in Fig. 8a. However, before the mass and momentum equations can be coupled with Eq. (3), the level set field variable must be made continuous over the fluid interfaces. This requires a time-dependent solution of the level set equation independent of the pressure and velocity fields. The modified version of the level set equation is shown in Eq. (4), where the velocity term has been dropped. COMSOL recommends the time-dependent solution of this equation for the $\varphi$-field at time $t \approx 5\varepsilon_{ls}/\gamma$ be used as the initial distribution of $\varphi$ for the solution of the coupled equations. A typical solution at this time is shown in Fig. 8b.

$$\frac{\partial \varphi}{\partial t} = \gamma \nabla \cdot \left[ \varepsilon_{ls} \nabla \varphi - \varphi(1 - \varphi) \frac{\nabla \varphi}{|\nabla \varphi|} \right] \tag{4}$$

### 3.3. Boundary conditions

Fig. 9 shows the boundaries associated with the model geometry. These labels are defined in Table 1. At all unlabeled internal boundaries, a continuity conditions are applied, insuring subdomain connectivity.

A symmetry condition is applied to all points at $r = 0$ in the geometry. In addition to constraining radial velocity, this condition also ensures that the stresses in the *z*-direction are diminished (to avoid singularity).

For the inlet boundary, a fundamental consideration when modeling actuation is that no net mass is added to or removed from the system. In this simulation, this is accomplished by having the integral of positive pressures equal the integral of the negative pressures over time.

Furthermore, the time dependent waveform for each method can be extrapolated from an understanding of how the squeeze-mode piezo actuates the system. As shown in Fig. 10a, in its simplest operation, the piezo contracts around the capillary, increasing the fluid chamber pressure. Once maximum contraction is reached,

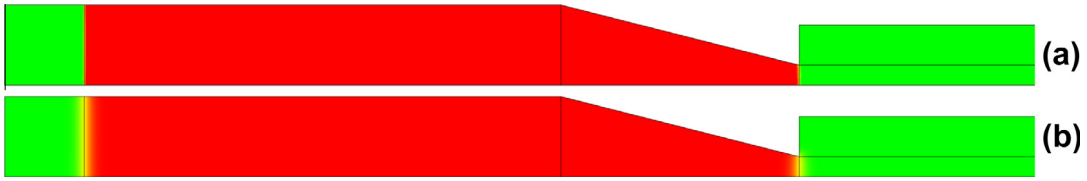


**Fig. 8.** Initial fluid distribution (a) before level-set initialization and (b) after level-set initialization.

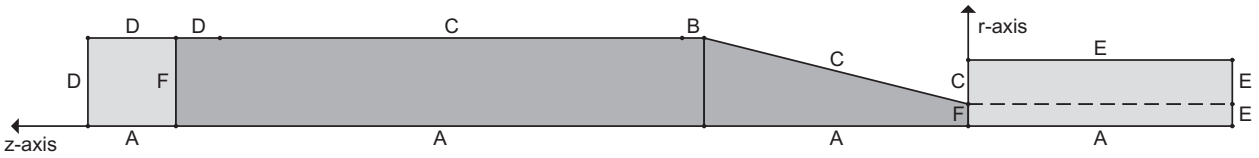


**Fig. 9.** Multi-phase flow model boundaries.

**Table 1**
Multi-phase flow model boundary types.

| | Boundary type | Equations |
|---|---|---|
| A | Symmetry – axial | $u_r = 0$ |
| B | Inlet – pressure, no viscous stress | $p$ = pressure<br>$[\mu(\nabla \boldsymbol{u} + (\nabla \boldsymbol{u})^T)]\boldsymbol{n} = 0$<br>$\varphi = 0$ |
| C | Wall – no-slip | $\boldsymbol{u} = 0$ |
| D | Wall – wetted | $\boldsymbol{n} \cdot \boldsymbol{u} = 0$<br>$\boldsymbol{F}_{fr} = -\frac{\mu}{\beta}\boldsymbol{u}$ |
| E | Outlet – pressure, no viscous stress | $p = 0$<br>$[\mu(\nabla \boldsymbol{u} + (\nabla \boldsymbol{u})^T)]\boldsymbol{n} = 0$ |
| F | Initial interface | $\varphi_0 = 0.5$ |

the piezo re-expands back to its original undeformed state. Fig. 10b illustrates the pressure waveform, with the magnitude of the waveform taken as a design parameter, and the period of the waveform as 8 μs. This analysis was verified using a single-phase fluid–structure interaction, described in Section 3.6.

A wetted wall is utilized when the fluid interface is expected to move along the wall. Two parameters are associated with this condition: slip length $\beta$ and contact angle $\theta_w$. $\beta$ defines the frictional force encountered by the fluid moving along the wall. In these simulations, the slip length couples to the mesh size at each node. The contact angle is used in an additional boundary calculation relating to surface tension. In all simulations, a contact angle of $\pi/2$ is used.

A pressure-based outlet boundary condition is used at two sides of the gas domain downstream of the nozzle. This allows the droplet to move through the gas domain without encountering boundary layer effects that would be present if a wall were modeled instead. This also reduces the need for a wide downstream region, the model's computational complexity.

The initial interface condition marks the fluid boundaries before the initialization step described in the previous subsection. It sets the boundary's initial equal to 0.5, which "seeds" the formation of a continuous distribution of $\varphi$ along a continuous step function, as shown in Fig. 8b.

### 3.4. Mesh

A triangular unstructured mesh is used in this model, shown in Fig. 11. The mesh is refined in areas in which a fluid interface is expected to move; specifically, in the gas region of the fluid reservoir and the gas region downstream of the nozzle.

The triangular mesh type was found to be superior to both structured and unstructured quadrilateral meshes in terms of efficiency and stability. Compared to the structured quad mesh, the unstructured triangular mesh requires significantly fewer elements to achieve similar results, providing greater computational efficiency. Compared to the unstructured quad mesh, the simulation solved more readily; there were several cases where singularities stop the simulation using the unstructured quad mesh that would not occur when an identical simulation was performed using the triangular mesh.

### 3.5. Solver parameters

The solution to this simulation is composed of two steps: initialization and time-dependent solving. As discussed in the Section 3.2.2, initialization is necessary to create a smooth $\varphi$-field.

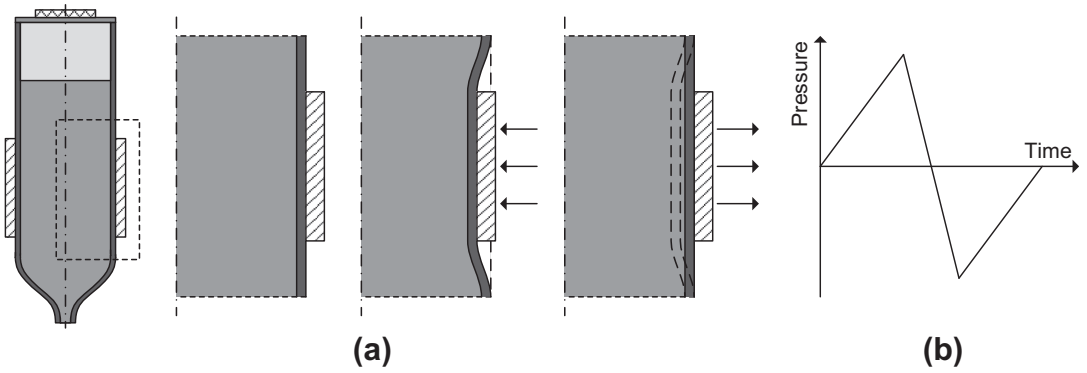


**Fig. 10.** (a) Actuation mechanism and (b) pressure waveform.

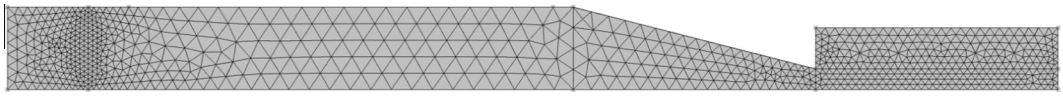

**Fig. 11.** Multi-phase flow model mesh.

During initialization, only $\varphi$ is solved for using Eq. (4) to create this smooth field. After initialization, the coupled conservation equations (mass, momentum and level set variable – Eqs. (1)–(3)) are solved simultaneously for $\varphi$, $p$ and $\boldsymbol{u}$. To solve these equations, two tools are needed: a time-stepping algorithm and a nonlinear solver. For time stepping, the generalized-$\alpha$ method was chosen. For nonlinear solving, the SPOOLES solver was chosen.

Both were chosen based on preliminary simulations using the suite of different solvers available in COMSOL. Generalized-$\alpha$ allowed for longer time steps and was less divergent than the BDF time stepping algorithm. The simulation had far less than 100,000 degrees of freedom (11,196 for the time-dependent solver), allowing for a Direct-type solver to be used as a non-linear solver (as opposed to an Iterative-type solver). Of the three Direct solvers available (SPOOLES, PARADISO and MUMPS), SPOOLES provided the fastest solutions of the three, with all three producing the same results.

### 3.6. Actuation boundary condition verification

A single-phase flow FSI COMSOL [47] model was also generated to ensure the pressure boundary condition could accurately approximate the pressure fluctuations caused by a capillary acting on a similarly structured fluid reservoir. Fig. 12a shows the geometry of the FSI model utilized. The dimensions of the fluid chamber are identical to those of the fluid reservoir of the multi-phase flow model, and the capillary wall thickness was chosen based on commercial squeeze-mode generators. The solid capillary is borosilicate, and as in the multi-phase model, the liquid is water.

Fig. 12b shows the six boundary conditions used in the model, and Table 2 specifies each. As before, the axial boundary ensures singularities are avoided at the axis of rotation. The open boundary allows flow into and out of the boundary, based on the generated velocities and pressures within the model. The fluid–solid interface couples the interface motion and stresses (note: the solid model treats $\boldsymbol{u}_s$ as a vector of displacements, while the fluid model treats $\boldsymbol{u}_f$ as a vector of velocities). The fixed boundary prevents displacement of the solid at the boundary. The boundary load applies a force that may vary in time and space. For this simulation, a pulse of force was applied from $z = 250$ μm to $z = 450$ μm over the span of 8 μs utilized in the previous simulation. Each step was modeled as a second-order continuous Heaviside function to ensure numerical stability.

Fig. 12c shows the mesh utilized with this model. An unstructured triangular mesh was generated, with a higher element density required at the fluid–solid interface and in the fluid itself.

Fig. 13 shows a comparison between the approximated pressure profile in the multi-phase flow model (a) and the modeled pressure distribution in the FSI model (b). It can be seen that there exists a strong correspondence between the two models, with only two slight differences utilized to improve numerical stability. When the variable pressure boundary condition was centered along the fluid chamber, the local pressure gradients at the pair of discontinuities caused the model to diverge. However, abutting the boundary against the flow focusing region improved solution. Furthermore, in the FSI model, during retraction, the negative pressure increases at a slower rate, then rapidly decreases. As before, this adjustment was made based on numerical stability in the model, defining the pressure in three stages as opposed to four.

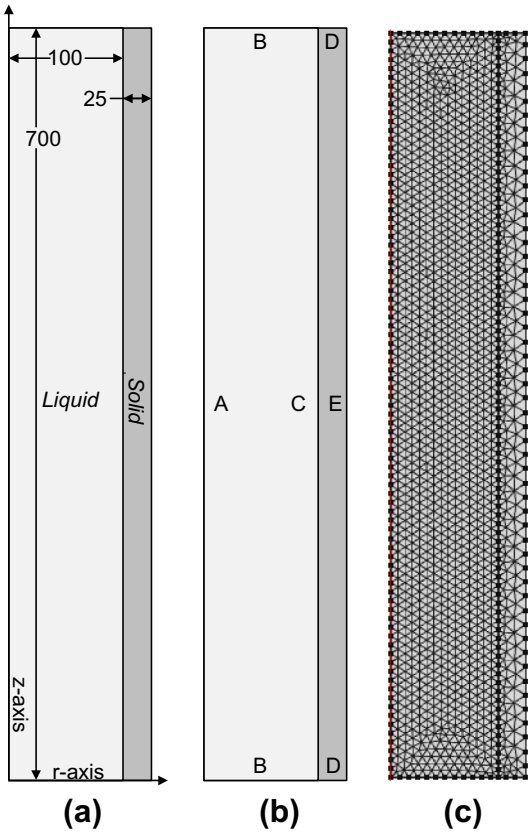


**Fig. 12.** Fluid–structure interaction model (a) geometry (dimensions in micrometers), (b) boundary conditions, (c) mesh.

**Table 2**
Fluid–structure interaction model boundary types.

| | Boundary type | Equations |
|---|---|---|
| A | Symmetry – axial | $u_r = 0$ |
| B | Open boundary | $[\mu(\nabla \boldsymbol{u} + (\nabla \boldsymbol{u})^T)]\boldsymbol{n} = 0$ |
| C | Fluid–solid interface | $\boldsymbol{u}_f = \dot{\boldsymbol{u}}_s$ $[-p\boldsymbol{I} + \mu(\nabla \boldsymbol{u}_f + (\nabla \boldsymbol{u}_f)^T)] \cdot \boldsymbol{n} = \boldsymbol{\sigma} \cdot \boldsymbol{n}$ |
| D | Fixed boundary | $\boldsymbol{u}_s = 0$ |
| E | Boundary load | $\boldsymbol{F} = \boldsymbol{f}(t)$ |

## 4. Simulations and analysis

The multi-phase flow FEA model described in the previous section was solved for varying pressure magnitudes at the inlet boundary condition. Depending on the applied pressure, there was one of two results, as shown in Fig. 14. The first result produces no generation. This occurs when the pressure magnitude lies below some critical value. A droplet may form at the nozzle, but insufficient inertia exists to overcome the viscous force/surface tension. The second result produces successful generation, which occurs when the pressure magnitude exceeds the critical value. This causes a droplet to form at the nozzle during the positive

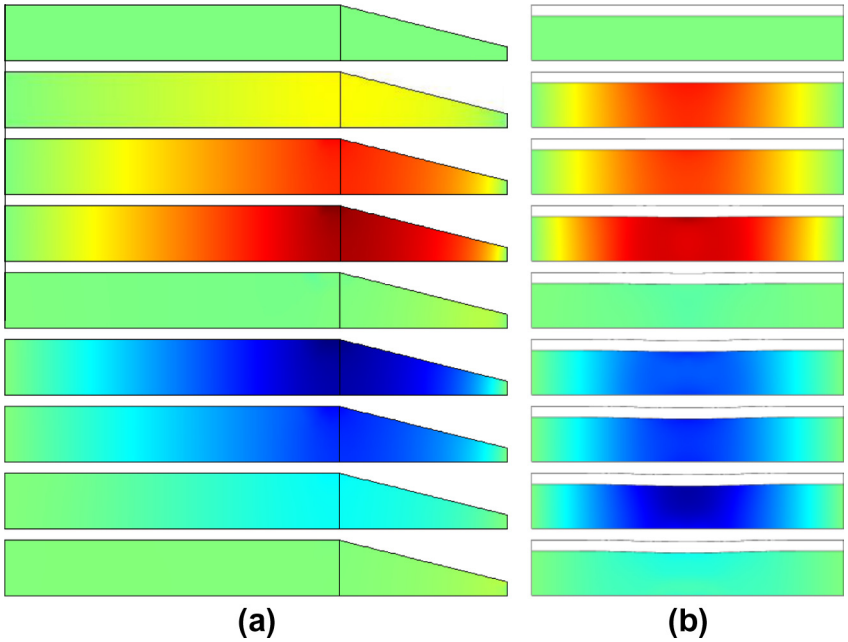


**Fig. 13.** Comparison of (a) modeled pressure variations in the gas reservoir, and (b) FSI pressure variations. In each model, red is positive pressure, blue is negative pressure and green is atmospheric pressure ($p = 0$ Pa). (For interpretation of the references to color in this figure legend, the reader is referred to the web version of this article.)

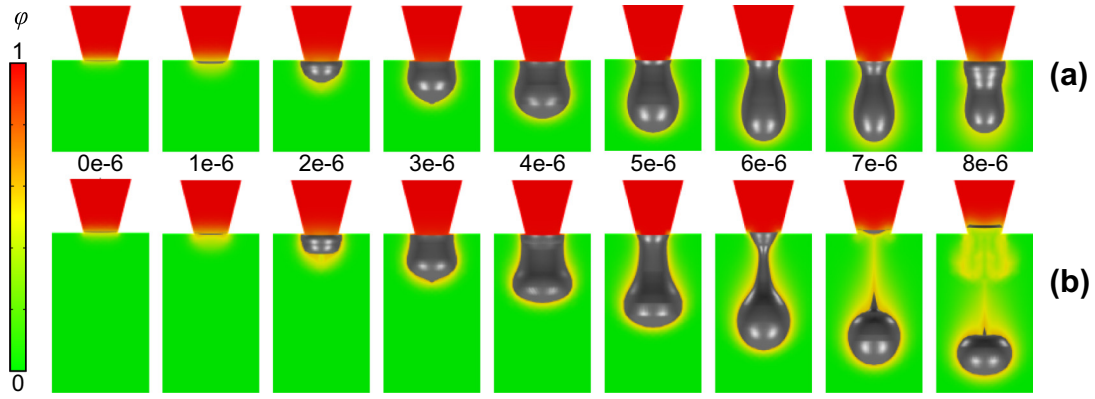


**Fig. 14.** Simulation visualizations of the level-set $\varphi$ scalar field for: (a) no generation – actuation pressure magnitude 1.0 MPa, (b) successful generation – actuation pressure magnitude 1.4 MPa. The gray droplet is the 3D surface for which level set variable is $\varphi = 0.5$ .

pressure regime, and then continue moving away from the nozzle during negative pressure, breaking away the droplet from the liquid reservoir.

The critical pressure for transitioning from no generation to successful generation was found to be between 1.2 and 1.3 MPa.

Based on these results, boundary pressure magnitudes in the range of 1.0–1.8 MPa were simulated and analyzed to explore the behavior of the pressure air gap in both regimes.

Fig. 15 shows the pressure profiles of the gas over time for three different actuation pressure magnitudes. The first, $p_{mag} = 1.0$ MPa, occurs in the no generation regime, while the other two, $p_{mag} = \{1.3, 1.5\}$ MPa, cause a droplet ejection. As can be seen, the shape of the gas reservoir pressure in the gap remains approximately the same regardless of actuation magnitude; however, the maximum pressure reached by the gas increases and occurs later in the actuation cycle as the actuation magnitude increases. In each case, it also appears the pressure slowly tapers off beyond the maximum value. Toward the end of the actuation cycle, the pressure boundary condition exerts a low pressure on the liquid reservoir, ending at 0 Pa at $t = 8$ μs and remaining zero for all future $t$. Holding the reservoir at this constant pressure differs from how the system would actually behave, where the direct effects of the actuator on the system would end at the end of the actuation period. But because this consideration occurs after the maximum pressure, it still allows the maximum pressure reached by this gas reservoir to be correlated to the droplet volume produced.

If only actuation pressures that generate droplets are considered, droplet volumes may also be extracted from the model. Fig. 16 shows a pair of plots with the maximum gas reservoir pressure and droplet volume at increasing values of the actuation pressure magnitude. As expected, both values increase as pressure increases: the former due to the greater pressure on the gas reservoir by the liquid, the latter due to the greater liquid volume pushed out during the transition from high pressure to low. This increase is linear in both cases, though there is a slight outlier at $p = 1.5$ MPa for droplet volume. Fig. 17 relates these two extrapolated quantities to one another, and a nearly linear correlation can be seen. This linear relationship provides a simple mechanism for indirectly detecting droplet size by measuring the maximum gas reservoir pressure.

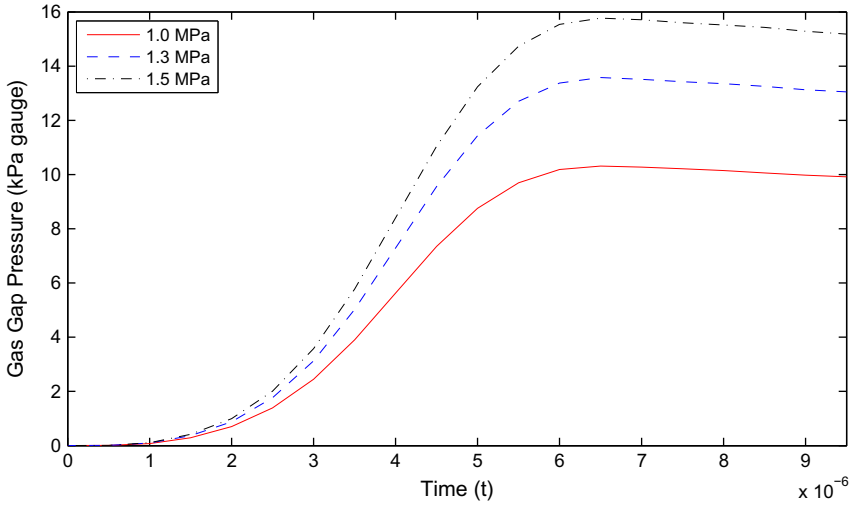


**Fig. 15.** Gas reservoir pressure during actuation.

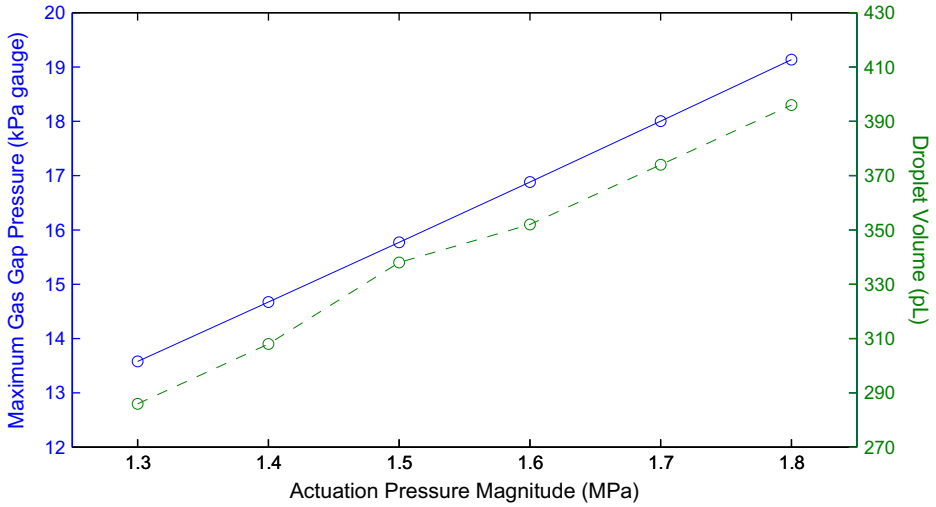


**Fig. 16.** Maximum gas reservoir pressures and droplet volumes at varying actuation pressure magnitudes.

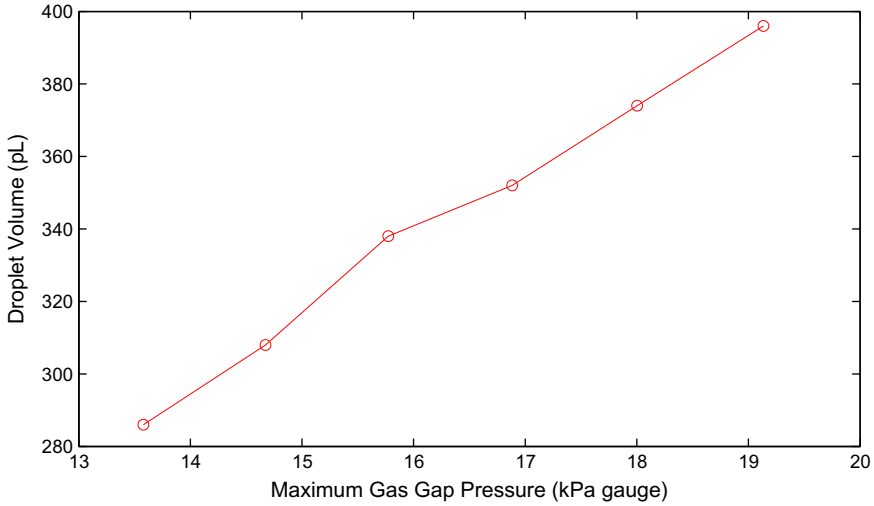


**Fig. 17.** Dependence of droplet volume on maximum gas reservoir pressure.

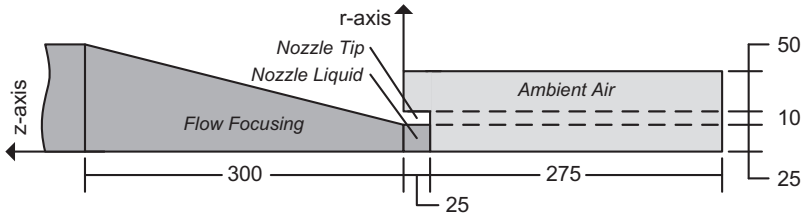


**Fig. 18.** Modification to model geometry to simulate nozzle region (dimensions in micrometers).

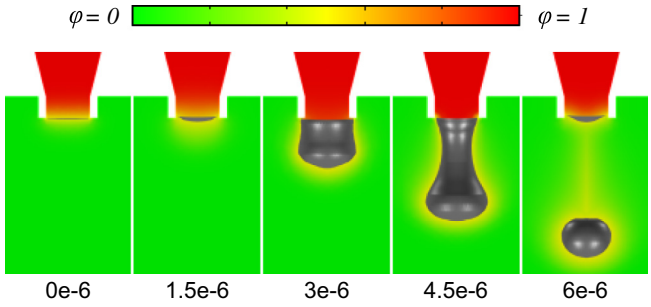


**Fig. 19.** Simulation visualizations of the level-set $\varphi$ scalar field for droplet generation with nozzle region – actuation pressure magnitude: 2.4 MPa.

In addition, a simulation was run demonstrating the effect of a nozzle on the results of the simulation (with the air area surrounding the nozzle area). Fig. 18 shows the modification to the geometry of the model: a 25 μm by 25 μm fluid region was added downstream of the flow focusing region. The solid nozzle tip was modeled as a 'notch' separating the ambient air from the nozzle liquid (the 'Nozzle Tip' in Fig. 18). Fig. 19 shows the droplet formed in response to a 2.4 MPa magnitude actuation of the form shown in Fig. 10.

Two key differences from the successful generation shown in Fig. 14 may be observed. First, the nominal actuation pressure magnitude for the simulation with the additional nozzle region included is higher. This is to be expected – the nozzle will increase the resistance against the motion of the fluid as it leaves the reservoir. Therefore, additional force will be required to create the droplet. Second, it is noted that the droplet forms more quickly in this simulation than the previous. As a result of this higher pressure, once the liquid overcomes the resistance in the nozzle, the droplet will form more quickly during the positive pressure portion of the actuation. During negative pressure, the increased magnitude will shear the droplet more quickly, resulting in a shorter ejection time for the droplet.

## 5. Conclusion

The current shortcomings in closed-loop droplet generation – measuring their volume in real-time and using that measurement to adjust the dispensing parameters for subsequent generation cycles – present a critical gap in current microfluidic technologies. In this paper, a concept was proposed and tested through simulation for integrating sensing into a droplet generator. This sensing will allow the measurement of the dispensed droplet volume in real-time by monitoring the pressure of a gas in the generator's fluid reservoir. The FEA simulations performed validated this connection between pressure and droplet volume and showed that it was linear.

Future work will incorporate fluid–structure interaction and a piezoceramic actuator model in the multi-phase flow simulations in order to better understand the relationship between the voltage waveform parameters applied to the piezo and the droplet volume/gas gap pressure. This will eventually lead to a virtual prototype that will incorporate a numerical controller to adjust actuation parameters of the piezo based on the droplet generated in the previous step. The final goal of this research will be to translate these simulations into a working device, and incorporate an array of these systems into a platform for various applications, such as DNA microarraying, tissue engineering and micromanufacturing.

## References

[1] Rayleigh JWS. On the instability of jets. Proc Lond Math Soc 1878;10:4–13.
[2] Zoltan SI. Pulsed droplet ejecting system. US patent 3683212; 1972.
[3] Kyser EL, Sears SB. Method and apparatus for recording with writing fluids and drop projection means therefor. US patent 3946398; 1976.
[4] Endo I, Sato Y, Saito S, Nakagiri T, Ohno S. Liquid jet recording process and apparatus therefor. UK patent 2007162; 1979.
[5] Vaught JL, Cloutier FL, Donald DK, Meyer JD, Tacklind CA, Taub HH. Thermal ink jet printer. US patent 4490728; 1984.
[6] Ben-Tzvi P, Rone W. Microdroplet generation in gaseous and liquid environments. Microsyst Technol 2010;16(3):333–56.
[7] Ahamed MJ, Gubarenko SI, Ben-Mrad R, Sullivan P. A piezoactuated droplet-dispensing microfluidic chip. J Microelectromech Syst 2010;19:110–9.
[8] Kim KT, Park YW. Feasibility of low-cost microarray printing with inkjet printer. Int Conf Control Autom Syst 2008:1932–5.
[9] Wu HC, Lin HJ, Hwang WS. A numerical study of the effect of operating parameters on drop formation in a squeeze mode inkjet device. Model Simul Mater Sci Eng 2005;13:17–34.
[10] Fan KC, Chen JY, Wang CH, Pan WC. Development of a drop-on-demand droplet generator for one-drop fill technology. Sens Actuators A Phys 2008;147:649–55.
[11] Brünahl J, Grishin A. Piezoelectric shear mode drop-on-demand inkjet actuator. Sens Actuators A Phys 2002;101:371–82.
[12] Tseng FG, Kim CJ, Ho CM. A high-resolution high frequency monolithic top-shooting microinjector free of satellite drops—Part I: concept, design and model. J Microelectromech Syst 2002;11:427–36.
[13] Dadvand A, Khoo BC, Shervani-Tabar MT. A collapsing bubble-induced microinjector: an experimental study. Exp Fluids 2009;46:419–34.
[14] Cabal A, Ross DS, Lebens JA, Trauernicht DP. Thermal actuator with optimized heater for liquid drop ejectors. Sens Actuators, A Phys 2005;123–124:531–9.
[15] Castrejón-Pita JR, Martin GD, Hoath SD, Hutchings IM. A simple large-scale droplet generator for studies of inkjet printing. Rev Sci Instrum 2005;79:075108.
[16] Amirzadeh-Goghari A, Chandra S. Producing droplets smaller than the nozzle diameter by using a pneumatic drop-on-demand droplet generator. Exp Fluids 2008;44:105–14.
[17] Nguon B, Jouaneh M. Design and characterization of a precision fluid dispensing valve. Int J Adv Manuf Technol 2004;24:251–60.
[18] Kamisuki S, Hagata T, Tezuka C, Nose Y, Fujii M, Atobe M. A low power, small, electrostatically driven commercial inkjet head. Int Worksh MEMS 1998:63–8.
[19] Kamisuki S, Fujii M, Takekoshi T, Tezuka C, Atobe M. A High-resolution, electrostatically driven commercial inkjet head. Int Conf MEMS 2000:793–8.
[20] Kim SJ, Song YA, Skipper PL, Han J. Electrohydrodynamic generation and delivery of monodisperse picoliter droplets using a poly(dimethylsiloxane) microchip. Anal Chem 2006;78:8011–9.
[21] Lee CH, Lal A. Single microdroplet ejection using an ultrasonic longitudinal mode with a PZT/tapered glass capillary. IEEE Trans Ultrason Ferroelectr Freq Control 2004;51:1514–22.
[22] Berggren WT, Westphall MS, Smith LM. Single-pulse nanoelectrospray ionization. Anal Chem 2002;74:3443–8.
[23] Koltay P, Birkenmeier B, Steger R, Sandmaier H, Zengerle R. Massive parallel liquid dispensing in the nanoliter range by pneumatic actuation. Int Conf New Actuators 2002:235–9.
[24] De Heij B, Van Der Schoot B, Bo H, Hess J, De Rooij NF. Characterization of a fL droplet generator for inhalation drug therapy. Sens Actuators A Phys 2000;85:430–4.
[25] Ernst A, Streule W, Schmitt N, Zengerle R, Koltay P. A capacitive sensor for non-contact nanoliter droplet detection. Sens Actuators A Phys 2009;153:57–63.

[26] Chang TN, Parthasarathy S, Wang T, Gandhi K, Soteropoulos P. Automated liquid dispensing pin for DNA microarray applications. IEEE Trans Autom Sci Eng 2006;3:187–91.
[27] Szita N, Sutter R, Dual J, Buser RA. A micropipettor with integrated sensors. Sens Actuators A Phys 2001;89:112–8.
[28] Wei J, Yue C, Chen ZL, Liu ZW, Makinwa KAA, Sarro PM. Implementation and characterization of a femto-farad capacitive sensor for pico-liter liquid monitoring. In: Proc Eurosensors XXIII; 2009. p. 120–3.
[29] Wassink MG. Inkjet printhead performance enhancement by feedforward input design based on two-port modeling. PhD dissertation, delft university of technology; 2007.
[30] Moore SK. Making chips to probe genes. IEEE Spectr 2001;38:54–60.
[31] Schena M, Heller RA, Theriault TP, Konrad K, Lachenmeier E, Davis RW. Microarrays: biotechnology's discovery platform for functional genomics. Trends Biotechnol 1998;16:301–6.
[32] Zhang M, Ma O, Diao X. Dynamics modeling and analysis of inkjet technology-based oligo DNA microarray spotting. IEEE Trans Autom Sci Eng 2006;3:159–68.
[33] Cooley P, Wallace D, Antohe B. Applications of ink-jet printing technology to biomems and microfluidic systems. Proc SPIE Conf Microfluid BIOMEMS 2001;4560:177–88.
[34] Aderogba S, Meacham JM, Degertekin FL, Fedorov AG, Fernandez F. Nanoelectrospray ion generation for high-throughput mass spectrometry using a micromachined ultrasonic ejector array. Appl Phys Lett 2005;86:203110.
[35] Ekström S, Önnerfjord P, Nilsson J, Bengtsson M, Laurell T, Marko-Varga G. Integrated microanalytical technology enabling rapid and automated protein identification. Anal Chem 2000;72:286–93.
[36] Yuan S, Zhou Z, Wang G, Liu C. MEMS-based piezoelectric array microjet. Microelectron Eng 2003;66:767–72.
[37] Stachowiak JC, von Muhlen MG, Li TH, Jalilian L, Parekh SH, Fletcher DA. Piezoelectric control of needle-free transdermal drug delivery. J Control Release 2007;124:88–97.
[38] Perçin G, Lundgren TS, Khuri-Yakub BT. Controlled ink-jet printing and deposition of organic polymers and solid particles. Appl Phys Lett 1998;73:2375–7.
[39] De Gans BJ, Duineveld PC, Schubert US. Inkjet printing of polymers: state of the art and future developments. Adv Mater 2004;16:203–13.
[40] Hebner TR, Wu CC, Marcy D, Lu MH, Sturm JC. Ink-jet printing of doped polymers for organic light emitting devices. Appl Phys Lett 1998;72:519–21.
[41] Szczech JB, Megaridis CM, Gamota DR, Zhang J. Fine-line conductor manufacturing using drop-on-demand PZT printing technology. IEEE Trans Electron Packag Manuf 2002;25:26–33.
[42] Lee TM, Kang TG, Yang JS, Jo JD, Kim KY, Choi BO, et al. 3D metal microstructure fabrication using a molten metal dod inkjet system. Int Solid-State Sens Actuators Microsyst Conf 2007:1637–40.
[43] Sui G, Leu MC. Investigation of layer thickness and surface roughness in rapid freeze prototyping. ASME J Manuf Sci Eng 2003;125:556–63.
[44] GeSiM, mBH. <http://www.gesim.de>.
[45] Ben-Tzvi P, Ben Mrad R, Goldenberg AA. A conceptual design and fe analysis of a piezoceramic acutated dispensing system for microdrops generation in microarray applications. Mechatron 2007;17:1–13.
[46] COMSOL Multiphysics, version 4.0a, COMSOL, Inc., <http://www.comsol.com>.
[47] COMSOL Multiphysics, version 4.2, COMSOL, Inc., <http://www.comsol.com>.